Chemical Science

ROYAL SOCIETY OF CHEMISTRY

EDGE ARTICLE

View Article Online
View Journal

Open Access Article. Published on 09 December 2025. Downloaded on 1/9/2026 8:12:14 PM.
This article is licensed under a Creative Commons Attribution-NonCommercial 3.0 Unported Licence.

Check for updates

Cite this: DOI: 10.1039/d5sc08182c

All publication charges for this article have been paid for by the Royal Society of Chemistry

Orientation of surface-immobilized DNA tetrahedron nanostructures dictates cell–material interaction

Haozhen Yu,† Haoyue Lv,† Ziyi Zhao, Siyi Duan, Xiaoman Duan and Biwu Liu *

Received 23rd October 2025
Accepted 30th November 2025

DOI: 10.1039/d5sc08182c

rsc.li/chemical-science

The versatile chemistry of DNA nanostructures enables the development of spatially controlled hybrid nanomaterials for applications in biosensing and nanomedicine. Despite extensive progress, precise control over their cellular interactions remains challenging. Here, we demonstrate a strategy that harnesses DNA NS with prescribed orientations on various materials to modulate the cellular interaction. Using spherical polystyrene nanoparticles, we demonstrate that DNA tetrahedron nanostructures (TDNs) with corner-protruding geometry enhance uptake efficiency by up to 8.4-fold. Mechanistic studies reveal that TDN orientation modulates configuration entropy at the cell–material interface, with vertex-aligned TDNs reducing entropy penalties to optimize receptor engagement. Moreover, tailoring TDN orientations serves as a general strategy to control cell–material interactions, as demonstrated with graphene oxides of varying sizes, enhancing their ability for membrane disruption and efficient cytoplasmic delivery. Overall, our findings establish TDN orientation as a design principle for tuning cell–material interactions, offering new opportunities for DNA-functionalized nanomaterials in nanomedicine, diagnostics, and biointerface engineering.

Introduction

The precise control of interactions between cells and nanoparticles (NPs) is fundamental to nanomedicine, biosensing, and environmental sciences, as these interactions regulate essential biological processes at the nano–bio interface.[1–6] Factors that affect cell–material interactions include size and shape,[7] surface charge,[8] hydrophobicity,[9] and surface ligands.[10,11] Among these, the spatial arrangement of surface ligands has become increasingly important for mimicking natural receptor–ligand systems, enhancing targeting precision, and reducing off-target effects.[12,13]

In this context, DNA nanostructures offer a highly promising platform for modulating cell–material interactions due to their programmability, biocompatibility, and precise spatial control over interaction sites and valences.[14] Of particular interest are DNA tetrahedron nanostructures (TDNs), which provide a rigid yet customizable framework for arranging functional molecules.[15–20]

Previous studies have demonstrated the integration of DNA TDNs with a range of nanomaterials, including synthetic polymer micelles,[21] gold NPs,[22] Fe_3O_4 NPs, quantum dots, microcapsules,[23] and metal–organic frameworks[24,25] for drug and nucleic acid delivery. Additionally, TDNs anchored on cell membranes have been employed for programmed cell–cell communication[26,27] and domain-specific interactions with cell membranes,[28] showing the versatility and broad potential of these nanostructures.[29]

Despite the promise of TDN-mediated ligand-receptor cellular internalization, few studies have addressed the intrinsic interactions between materials and cells when TDNs are immobilized on nanosurfaces. Free-floating TDNs engage cellular membranes through a "corner-attack" mode, facilitating caveolin-mediated endocytosis (CvME).[30–32] However, when immobilized on surfaces, TDNs may exhibit distinct modes of interaction with cells.[33–35] For example, TDNs anchored at fewer sites (*i.e.* presenting more exposed corners) may show enhanced cellular uptake due to the potential for multiple interactions.[36–38] Conversely, it is also possible that the higher charge density and steric hindrance associated with TDN lines/faces inhibit corner-mediated interactions with the cell membrane. Furthermore, in biological environments, free TDNs can adsorb nonspecifically onto surfaces, altering their spatial configuration and the manner in which they interact with cells.[39–42] Such alterations may shed light on discrepancies in cellular responses to DNA nanostructures.[43,44] Understanding and controlling the orientation of DNA nanostructures on surfaces are thus critical for systematically tuning cell–material interactions.

Herein, we present a strategy that modulates cell–material interactions by rationally varying the anchoring orientation of TDNs on surfaces without specific targeting agents (Fig. 1). By controlling the precise configuration of TDNs (line-, face-, or

Institute of Analytical Chemistry and Instrument for Life Science, The Key Laboratory of Biomedical Information Engineering of Ministry of Education, School of Life Science and Technology, Xi'an Jiaotong University, Xi'an, Shaanxi 710049, P. R. China. E-mail: biwuliu@xjtu.edu.cn

† H. Y. and H. L contributed equally to this work.

Open Access Article. Published on 09 December 2025. Downloaded on 1/9/2026 8:12:14 PM.
This article is licensed under a Creative Commons Attribution-NonCommercial 3.0 Unported Licence.

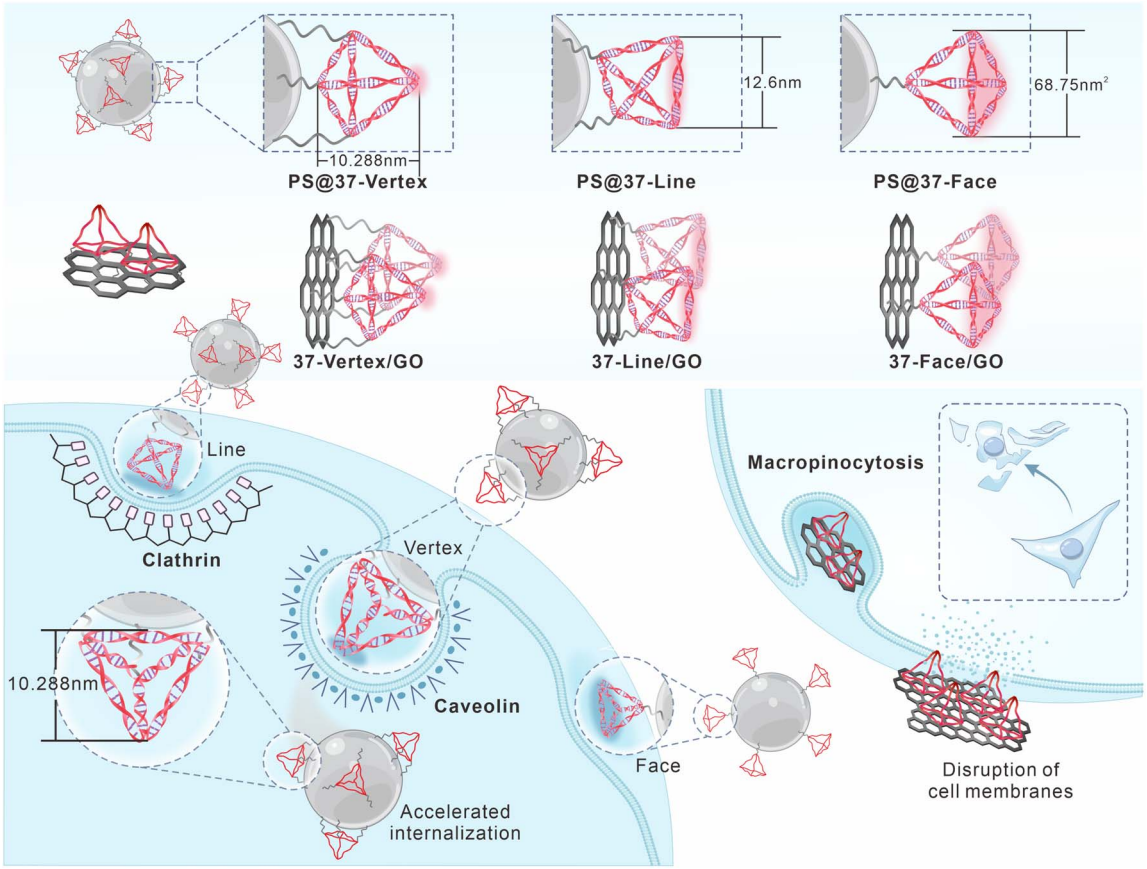

Fig. 1 Design principles of DNA tetrahedron-anchored materials interact with cells modulated by the orientation of TDNs. (Top) Oriented TDNs display distinct interaction geometries and surface areas, providing tunable modes for controlling cell–material interfaces. (Bottom) The TDN configurations enable specific cellular interactions, including enhanced clathrin or caveolin-mediated endocytosis for intracellular delivery, accelerated macropinocytosis *via* vertex-aligned TDNs, and controlled disruption of cellular membranes in large GO systems.

vertex-displayed), we demonstrate the ability to tune cellular uptake efficiency, endocytic mechanisms, and subcellular localization of both spherical polystyrene nanoparticles (PS NPs) and 2D graphene oxide (GO). Confocal microscopy and flow cytometry reveal over 8.4-fold differences in internalization efficiency between vertex-displayed PS@TDNs and face-displayed counterparts. Mechanistic studies further prove that vertex-oriented TDNs exploit a prescribed displaying of TDN corners to maximize interaction efficiency, utilizing diverse endocytic pathways and facilitating lysosomal escape. Additionally, we show that tuning TDN anchoring configurations can enhance the therapeutic potential of GO by improving its membrane rupture capabilities. These findings offer a powerful and versatile strategy for designing advanced DNA-functionalized nanomaterials with applications ranging from drug delivery to diagnostic technologies and biophysical studies of cellular mechanisms.

Results and discussion

Design and fabrication of oriented TDNs on nanosurfaces

TDNs can enter cells without additional transfection agents.[30–32] However, numerous studies have involved additional functional nanomaterials and cell-targeting elements for biomedical applications. Here, we focus on the intrinsic role of TDN orientation in dictating receptor binding and endocytic routing at the cell–material interface. By controlling whether TDNs are presented through vertices, edges, or faces, we aim to reveal how different anchoring geometries influence membrane recognition, uptake efficiency, and intracellular trafficking. This approach avoids confounding effects from auxiliary chemical modifications, thereby isolating the structural contribution of DNA frameworks. Such a strategy provides a mechanistic basis for understanding how nanoscale geometry governs cellular interactions of host materials.

To evaluate the efficacy of TDNs as artificial ligands for mediating material–cell interactions, we investigated two model systems: fluorescently labeled PS NPs and two-dimensional GO. We first examined PS NPs. Carboxylated PS NPs (*ca.* 100 nm) were labeled with fluorescein isothiocyanate (FITC) and conjugated with amine-functionalized DNA strands (cLinker-NH2, detailed in Table S1) using the NHS-EDC coupling chemistry. TDNs of two different sizes, TDN-17 and TDN-37, were used. We engineered three distinct anchoring strategies: Vertex (PS@TDN-Vertex), Line (PS@TDN-Line), and Face (PS@TDN-Face), corresponding to three-point, two-point, and one-point DNA overhang interaction, respectively (Fig. 1). These

 © 2025 The Author(s). Published by the Royal Society of Chemistry

Open Access Article. Published on 09 December 2025. Downloaded on 1/9/2026 8:12:14 PM.
This article is licensed under a Creative Commons Attribution-NonCommercial 3.0 Unported Licence.

configurations allow us to rationally investigate how the spatial organization of TDNs affects cellular uptake behaviors.

The successful assembly of TDNs was confirmed using agarose gel electrophoresis. Both TDN-17 and TDN-37 exhibited sharp migration bands, indicating precise folding and high structural purity (Fig. S1). Furthermore, atomic force microscopy (AFM) revealed that bare PS NPs exhibited smooth surfaces, while PS@TDNs displayed uniformly distributed protrusions originating from the DNA nanostructures (Fig. 2a). These surface modifications directly correlated with dynamic light scattering measurements, which showed increased hydrodynamic size upon TDN conjugation, and ζ-potential data indicating a shift to a more negative surface due to the polyanionic nature of DNA (Fig. S2). Importantly, the number of TDNs on each NP was controlled by adjusting reaction stoichiometry, yielding comparable TDN densities for all orientations and sizes (Fig. S3 and S4).

To ensure that TDNs were anchored on the particle surface, we centrifuged the mixture of PS NPs and TDNs (15 000 rpm, 15 min). The hybrid materials sedimented at the bottom, visualized through dual fluorescence signals: green (FITC-labeled NPs) and red (Cy5-labeled TDNs) (Fig. 2b). In contrast, free TDNs (no overhangs) failed to bind and remained in the supernatant, confirming specific hybridization *via* DNA oligo overhangs. To confirm that the vertex, line, and face orientations remained intact after immobilization, we performed a distance-dependent fluorescence-quenching assay on GO. While GO is a general quencher for many fluorophores, its quenching efficiency is strongly distance dependent. Three FAM-labeled TDN37 constructs with identical backbones (TDN37-Vertex-FAM, TDN37-Line-FAM, and TDN37-Face-FAM) were prepared. Each carried a 15-nt sticky end for GO-cDNA anchoring and a single FAM reporter positioned at the vertex opposite the anchoring site. Simple geometric estimates predicted distinct mean FAM–GO distances for the three orientations (Vertex ≈ 5.1 nm < Line ≈ 14.5 nm < Face ≈ 17.7 nm). Because the fluorophore was placed on the distal end of each TDN, the fluorescence of the GO/TDN complexes could be readily monitored. Under comparable surface coverages, the residual fluorescence (I/I_0) followed Face > Line > Vertex, confirming that these three spatial orientations were preserved on the GO surface (Fig. S5 and S6).

Next, we evaluated the stability of PS@TDNs in phosphate buffer saline (PBS) and cell culture medium over 24 h. While TDNs exhibited excellent stability in PBS, maintaining consistent fluorescence signals, significant fluorescence decay

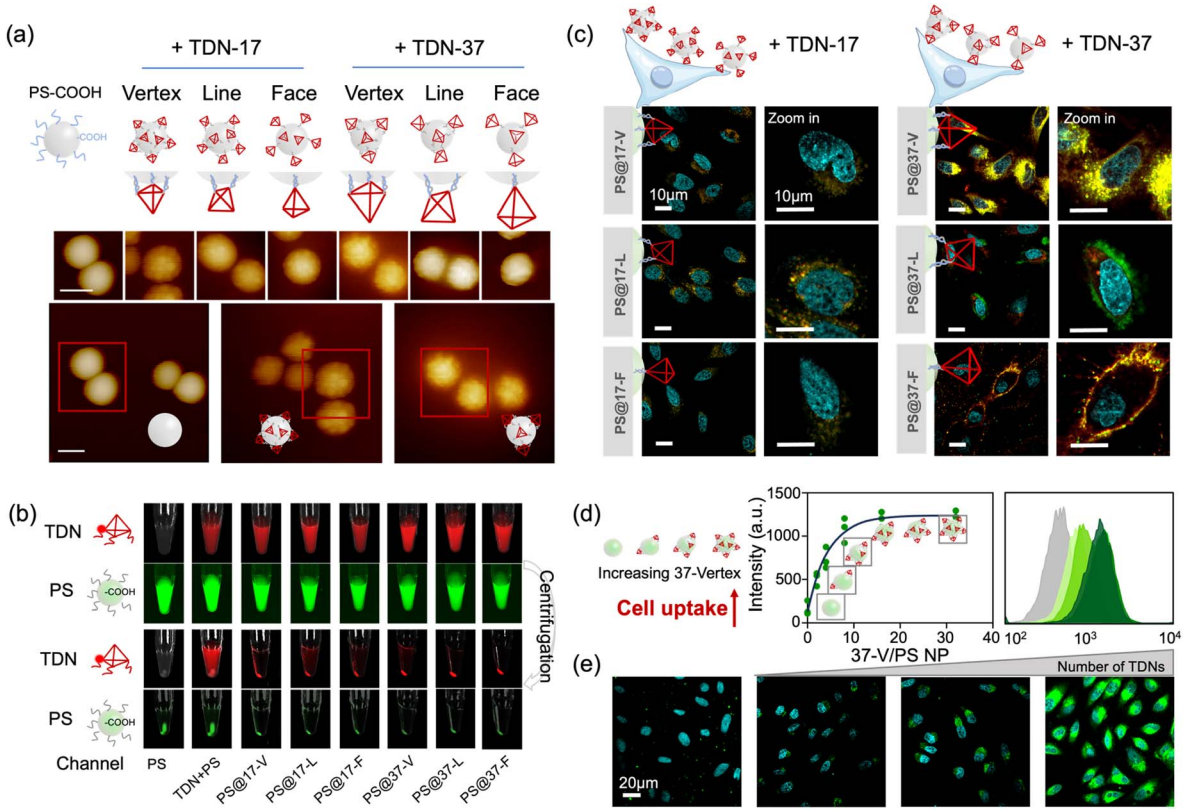

Fig. 2 Preparation and characterization of oriented TDN-anchored nanoparticles and their cellular uptake. (a) AFM images showing surface roughness of PS nanoparticles functionalized with TDNs of defined orientations and sizes (TDN-17 and TDN-37). (b) Fluorescence images of PS@TDNs before and after centrifugation (15 000 rpm, 15 min), confirming stable surface anchoring. (c) Confocal images of HeLa cells incubated with PS@TDN-17 and PS@TDN-37 prepared by three anchoring strategies for 4 h. (Left) Full-field images; (right) zoomed-in views. Scale bars, 10 μm. (d) Fluorescence measurement of PS@TDN37-1 uptake as a function of TDN loading. Uptake was quantified by flow-cytometry MFI ($n = 3$). The corresponding confocal images after 1 h incubation are shown in (e). Scale bars, 20 μm.

Open Access Article. Published on 09 December 2025. Downloaded on 1/9/2026 8:12:14 PM.
This article is licensed under a Creative Commons Attribution-NonCommercial 3.0 Unported Licence.

occurred in the cell culture medium during the first 6 h, gradually plateauing (~62% retained) (Fig. S7). This reduction is likely caused by partial degradation of the DNA structures, either by nucleases or through interactions with serum proteins. Notably, TDN-37 showed slightly higher stability compared to TDN-17, consistent with previous studies linking TDN size to enhanced structural durability. To minimize potential artifacts by TDN degradation-induced signal loss, we monitored the fluorescence of FITC-labeled PS NPs in the cellular uptake assays. Nevertheless, these results demonstrated that TDNs of controlled orientations and densities were successfully conjugated to PS NPs and remained sufficiently stable for cellular interaction studies.

Corner-protruding 3D geometry enabled efficient and rapid internalization

With well-controlled coverage of TDNs on PS NPs, we next investigated how TDN orientation regulates cellular uptake. Two sizes of TDNs (TDN-17 and TDN-37) and three anchoring modes (vertex, line, and face) were systematically evaluated. Cy5-labeled TDNs enabled fluorescence tracking, and uptake into HeLa cells was quantified by confocal microscopy and flow cytometry. After 4 h incubation, striking orientation-dependent differences were observed. For smaller TDN-17 (edge length *ca.* 6.1 nm), both vertex-anchored (PS@17-V, three anchoring sites) and line-anchored (PS@17-L, two anchoring sites) hybrids exhibited partial internalization, with PS@17-L showing a four-fold higher uptake compared to face-anchored hybrids (PS@17-F, one anchoring site) (Fig. 2c, left). In contrast, for larger TDN-37 (edge length ~10.3 nm), vertex-anchored hybrids (PS@37-V) displayed the most efficient uptake, markedly surpassing line- and face-anchored configurations (Fig. 2c, right). The superior performance of TDN-37 further underscores the corner-protruding advantage, which is amplified by its larger three-dimensional architecture. PS@37-L exhibited limited internalization, with most particles retained at the plasma membrane, while PS@37-F remained entirely membrane-bound. These results highlight the vertex-display geometry as the most favorable orientation, likely owing to its corner-protruding 3D structure that facilitates membrane engagement.

Interestingly, CLSM imaging revealed distinct intracellular distributions of Cy5-labeled TDNs and FITC-labeled PS NPs (Fig. 2c), suggesting the partial degradation of TDNs after internalization. We validated this by treating PS@TDNs with DNase I, which fully degraded the TDNs within 1 h (Fig. S8), consistent with previous reports. This degradation supports cargo release and is beneficial for delivery applications.

The density of TDNs on the particle surface strongly influenced uptake. Increasing the amount of TDN-37-Vertex produced a clear dose-dependent rise in flow-cytometry fluorescence (Fig. 2d). At the highest loading, PS@37-V showed an 8.4-fold enhancement in uptake relative to bare PS NPs with matched size and particle number after 2 h. CLSM confirmed this trend, showing much higher intracellular fluorescence for PS@TDNs (Fig. 2e, S9 and S10). FITC intensity therefore reflects particle number. Because the TDN shell gradually degrades in serum, all inhibitor and pathway studies were performed at 2 h to avoid contributions from late-stage degradation. Dye leakage from PS NPs was excluded, and PS@TDNs showed no detectable cytotoxicity (Fig. S11).

We next examined how TDN orientation affects uptake kinetics. PS@37-V internalized rapidly, with detectable entry within 5 min (Fig. 3a). Flow cytometry separated the six hybrids into fast and slow groups (Fig. 3b). PS@37-V, PS@17-L, and PS@17-V reached a plateau within 10 min, whereas PS@37-L, PS@37-F, and PS@17-F internalized slowly and remained near the membrane. After 6 h, PS@37-V, PS@17-L, and PS@17-V showed sustained uptake (Fig. 3c and S12). These results demonstrate that TDN geometry directly controls the rate and extent of internalization, with vertex presentation providing the strongest effect.

The observed differences in uptake efficiency and kinetics can be attributed to the unique interaction mechanisms of oriented TDNs with the cell membrane. Liang *et al.* previously demonstrated that a single TDN rapidly internalizes cells through a two-stage process: (1) random movement of TDNs bound to the cell membrane (>45 s) and (2) a rapid internalization phase (~15 s).[30] The distinct uptake behaviors can be explained by how oriented TDNs interact with the membrane. Liang *et al.* showed that free TDNs internalize through an initial membrane-bound diffusion phase followed by rapid entry. The sharp vertex of a TDN initiates contact and drives a "corner-attack" mode that favors endocytosis. On our PS NPs, PS@37-V followed a similar pattern: brief lateral movement on the membrane was followed by fast uptake (Fig. 3d and e). Immobilizing TDNs in a defined orientation restricts free rotation and maintains a fixed interaction axis, which increases the chance of vertex-mediated contact and accelerates membrane penetration.

Mechanistically, the vertex concentrates the interaction at one curved tip. This increases local contact pressure. It also lowers the bending-energy barrier needed for membrane wrapping. The exposed tip can reach beyond the steric and protein-corona layer to access receptors. The vertex forms a nanoscale hotspot that promotes receptor clustering. In contrast, line- and face-oriented TDNs spread force and ligands over larger areas. This reduces contact efficiency and raises the barrier for pit formation. These geometric effects explain the fast and efficient internalization of PS@37-V.

Orientation-dependent uptake pathways

The cellular uptake of nanomaterials is important for their downstream applications. For instance, Lesniak *et al.* showed that NP adhesion to the plasma membrane is a prerequisite for efficient internalization, underscoring the role of surface–membrane interactions.[30,45] In addition, recent work has demonstrated that nanoparticle shape modulates ligand–receptor dynamics and thereby alters uptake kinetics.[46] The cellular uptake of nanomaterials is closely tied to their downstream functions. Nanoparticle adhesion to the plasma membrane is often required for internalization, and particle shape can modulate receptor dynamics and uptake kinetics. We next examined the endocytic routes used by PS@TDNs using

 © 2025 The Author(s). Published by the Royal Society of Chemistry

Open Access Article. Published on 09 December 2025. Downloaded on 1/9/2026 8:12:14 PM.
This article is licensed under a Creative Commons Attribution-NonCommercial 3.0 Unported Licence.

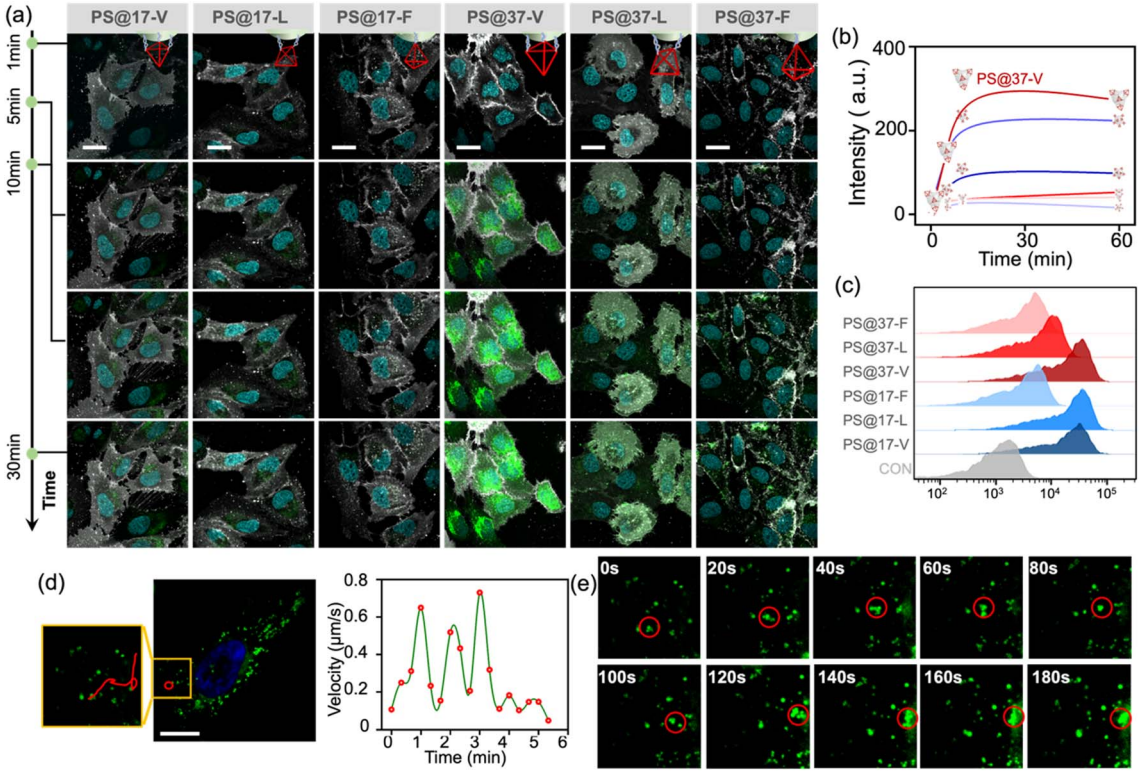

Fig. 3 Kinetic tracking of the TDN-mediated cellular uptake of PS NPs. (a) Confocal fluorescence images of HeLa cells incubated with PS@TDNs prepared by three anchoring methods at different time points. Cell membranes are labeled in white, and PS@TDNs are shown in green. Scale bars, 10 μm. (b) Quantification of the fluorescence intensity of PS NPs in HeLa cells. (c) Flow cytometry analysis of cellular fluorescence intensity after incubating HeLa cells with PS@TDNs using three anchoring methods for 6 h ($n = 3$ biologically independent experiments, each counting 10 000 cells). (d) Live-cell tracking of PS@TDNs (green) movement in HeLa cells. The magnified square region shows the trajectory of the particles. (e) Snapshots of live-cell tracking at different time points. Scale bars, 10 μm.

pharmacological inhibitors. HeLa cells were pre-treated with sucrose, methyl-β-cyclodextrin (MβCD), or cytochalasin D to inhibit clathrin-mediated endocytosis (CME), caveolin-mediated endocytosis (CvME), and macropinocytosis, respectively. After 30 min pretreatment, cells were incubated with PS@TDNs for 2 h and analyzed by confocal microscopy and flow cytometry.

The inhibition profiles differed across TDN orientations. Sucrose strongly reduced the uptake of PS@17-L, indicating CME dependence. In contrast, PS@37-V showed pronounced inhibition by MβCD, pointing to CvME as its primary route (Fig. 4a). Flow cytometry quantification supported these trends by normalizing mean fluorescence intensity to untreated controls. These results were highly reproducible across biological replicates, with rigorous quantitative characterization supporting the observed trends (Fig. S13).

$$\mathrm{IG} = 1 - \frac{\mathrm{MFI}_{\mathrm{inhibitor}}}{\mathrm{MFI}_{\mathrm{control}}}$$

To further assess endocytic pathways, we conducted flow cytometry and normalized the MFI to the control group. The inhibition grade (IG) was calculated using the formula mentioned above, with values ≤0 set to 0. A heatmap was generated to depict the dependency on different endocytic pathways, with darker colors indicating higher IG values (Fig. 4b). The results revealed that line-displayed PS@17-L predominantly utilized CME for internalization, with CvME and macropinocytosis also contributing to the uptake process (Fig. 4c). An analysis of face-displayed PS@TDNs, particularly PS@37-F, revealed minimal internalization, which aligns with the absence of structural features promoting membrane interactions. The flat orientation likely minimizes direct receptor engagement, thereby reducing uptake efficiency. Interestingly, such configurations, which exhibit low internalization, are still relevant in applications requiring cell membrane monitoring or the real-time study of intercellular signal transmission. Previous studies, such as the work by Le *et al.*,[41] have demonstrated that multivalent receptor–ligand interactions on larger face areas reduce ratios of membrane-adhered structures, further supporting the utility of face-displayed TDNs in applications where cell–material interactions should be minimized.[47]

The intracellular fate of nanoparticles is critical to their functionality in cargo delivery. To explore this aspect, we tracked the subcellular localization of PS@TDNs incubated with HeLa cells for 3 h (Fig. 4d). Green fluorescent PS NPs were used to visualize nanoparticles, while Hoechst 33342 and LysoTracker Red were employed to stain nuclei and lysosomes, respectively. Pearson correlation analysis quantified the colocalization of PS@TDNs with lysosomes, providing insight into lysosomal entrapment and potential escape. Vertex-displayed

Open Access Article. Published on 09 December 2025. Downloaded on 1/9/2026 8:12:14 PM.
This article is licensed under a Creative Commons Attribution-NonCommercial 3.0 Unported Licence.

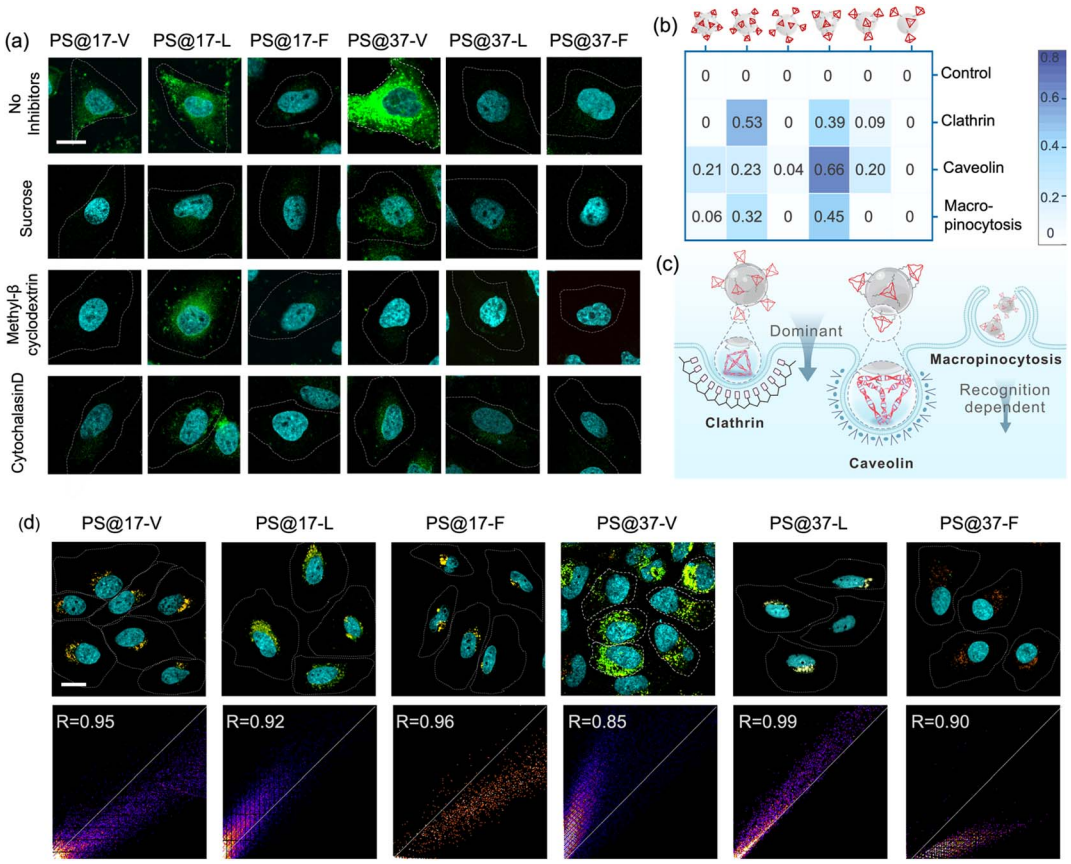

Fig. 4 Mechanistic investigation into the cell entry pathways of PS@TDNs. (a) Confocal microscopy images showing the uptake of PS@TDNs (green) with three different anchoring methods after treatment with four inhibitors. Scale bar, 10 μm. (b) Heat maps with IG values. Each cell shows an IG value, with higher values and darker colors indicating greater dependence. (c) Schematic of the endocytic pathways of PS@TDNs. (d) Confocal images show PS NPs (green), nuclei (blue), and lysosomes (orange). Pearson correlation analysis was performed, with a white line marking the areas of complete colocalization with lysosomes. The Pearson coefficient R-value is displayed on the image to indicate the degree of overlap. Scale bar, 10 μm.

PS@37-V demonstrated a lower Pearson correlation coefficient, suggesting a reduced tendency for lysosomal trapping and a higher likelihood of escape into the cytosol. This capacity for lysosomal escape is particularly advantageous for efficient cytosolic delivery of therapeutic molecules, such as drugs or genes. In contrast, PS@17-V, which showed significant reliance on CvME for internalization, demonstrated a stronger lysosomal correlation, indicating its potential for applications where lysosomal targeting is required. Face-displayed PS@37-F exhibited the highest lysosomal colocalization, consistent with its lower uptake efficiency and reduced reliance on non-lysosomal pathways.

An equally important finding is the applicability of specific TDN orientations for the selective modulation of cell–material interactions. While vertex-displayed TDNs demonstrated high uptake efficiency and lysosomal escape potential, face-displayed PS@TDNs minimized cell–material interactions, thereby demonstrating their utility in applications requiring reduced cellular entry. For instance, when lysosomal entrapment is desired, as in lysosome-targeted chimeric antigen receptor platforms, face-displayed PS@TDNs offer a promising solution. Similarly, membrane monitoring applications that require minimized cellular uptake would benefit from the reduced interaction profile of flat-oriented configurations. Overall, these findings highlight that TDN orientation governs not only the pathway of cellular uptake but also the intracellular fate of nanoparticles, providing a versatile platform for tuning cell–material interactions.

Oriented TDNs as a general strategy for cell–material interaction

Lastly, we demonstrate that our oriented TDNs can be used as a general strategy to facilitate the cell–material interactions. To this end, graphene oxide (GO) was selected as a model nanomaterial due to its unique two-dimensional structure and tunable surface chemistry. GO is widely used in drug delivery, bioimaging, biosensing, and targeted therapy.[48–50] Its interactions with cellular membranes are inherently complex and difficult to predict. Depending on its size, surface functionalization, and structural orientation, GO can exhibit a wide range of behaviors, including cellular uptake, membrane insertion, or even membrane disruption. GO below 500 nm and on the micrometer scale presents distinct opportunities and challenges in nanomedicine.

 © 2025 The Author(s). Published by the Royal Society of Chemistry

Open Access Article. Published on 09 December 2025. Downloaded on 1/9/2026 8:12:14 PM.
This article is licensed under a Creative Commons Attribution-NonCommercial 3.0 Unported Licence.

We hypothesize that oriented TDNs could modulate GO-cell interactions by leveraging the structural programmability of TDNs to control the endocytic pathways and intracellular fate of GO. We selected two different sizes of GO, 100 nm (small-sized GO, s-GO) and 300 nm (large-sized GO, l-GO), as these two size regimes offer fundamentally different interactions with cells, ranging from efficient internalization to membrane perturbation (Fig. 5a). S-GO primarily interfaces with cells *via* CME, making it an ideal candidate for intracellular delivery and bioimaging.

However, the efficiency of cellular internalization remains low for unmodified s-GO. To address this, we anchored TDNs, specifically with the 37-V orientation, onto the s-GO surface to maximize uptake efficiency (Fig. 5a and S14). Flow cytometry analysis confirmed that 37-V/s-GO significantly increased cellular uptake compared to other configurations and ssDNA-GO (Fig. 5b, left). The multivalent ligand presentation enabled by the 37-V configuration creates sharp, localized interaction points that enhance membrane adhesion and initiate endocytosis. In contrast, line- and face-displayed configurations exhibited diminished uptake efficiency, further supporting the advantage of the vertex orientation. Of note, the amount of TDNs loaded on GO was maintained similarly for different orientations (Fig. S15). Also, the size and ξ-potential measurements showed no significant differences for all TDN-GO, excluding the possible electrostatic interaction (Fig. S16 and S17).

Furthermore, TEM showed that GOs accumulated at the plasma membrane (Fig. 5c). They were also found inside typical macropinocytic structures. Intracellular vesicles with a macropinosome-like morphology were observed, indicating active macropinosome formation (Fig. S18). These features are consistent with enhanced actin polymerization and membrane wrapping induced by vertex-aligned TDNs. This process was initiated by the formation of cellular membrane ruffles, which, upon closure, internalized both 37-V/s-GO and extracellular fluid into the cell.[51] To further confirm the endocytic pathway, we treated cells with cytochalasin D, an inhibitor of actin polymerization, which is critical for macropinocytosis. Confocal imaging demonstrated a significant reduction in the internalization of 37-V/s-GO following cytochalasin D pretreatment (Fig. 5d), indicating that the macropinocytosis pathway is a key mediator for 37-V/s-GO uptake. This is a marked departure from the typically reported CME observed with unmodified s-GO, highlighting how oriented TDN configuration can reshape cellular engagement mechanisms. Importantly, cytotoxicity assays indicated minimal toxicity for all GO-bound TDN orientations, including 37-V/s-GO (Fig. 5b, right). This biocompatibility, combined with increased cellular uptake, positions 37-V/s-GO as an efficient nanovehicle for intracellular imaging and targeted delivery.

Additionally, l-GO provides a distinct opportunity to exploit its extensive basal plane for membrane interaction, such as mimicking the immunological synapses for T-cell activation, direct cytoplasmic delivery,[52] and disrupting bacterial membranes.[53] However, unmodified l-GOs often cause uncontrolled, nonspecific membrane adsorption. Rational engineering of DNA anchoring thus provides a unique means to impose spatial control over how GOs engage with cellular membranes. We hypothesized that 37-V anchoring could focus basal-plane interactions at sharp nanoscopic vertices, at working doses, amplifying local stress on the plasma membrane and enabling controlled, reversible disruption (Fig. 6a).

Lactate dehydrogenase (LDH) assays showed that 37-V/l-GO induced higher LDH release during the 2–6 h exposure window, indicating transient membrane permeabilization (Fig. 6b). Flow cytometry and confocal quantification further supported this result, revealing a threefold increase in cellular uptake compared with control configurations (Fig. 6c). TEM imaging

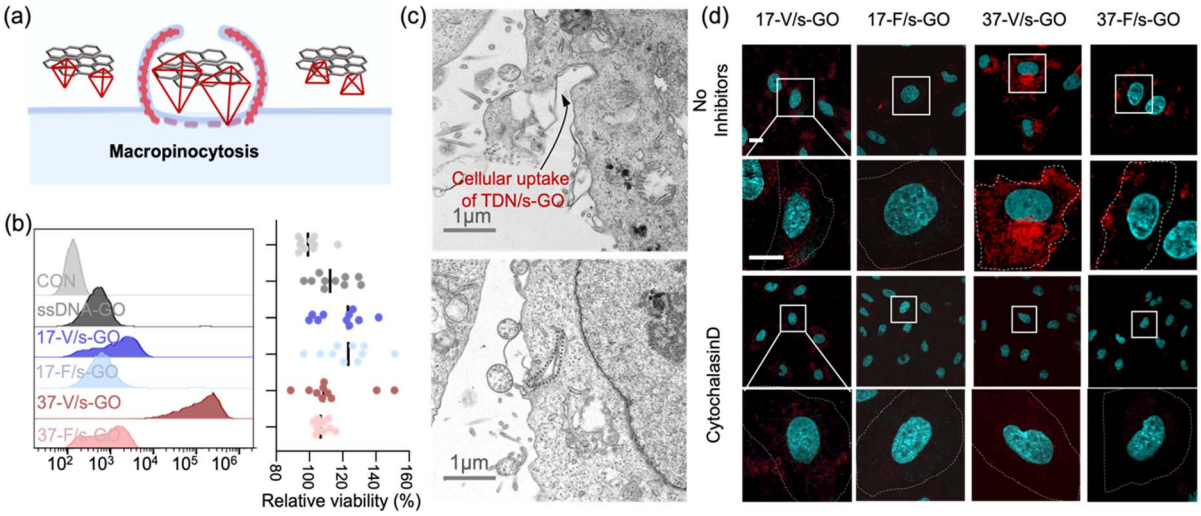

Fig. 5 Cellular internalization pathway of s-GO. (a) Schematic illustration of the s-GO internalization pathway. (b) (Left) Flow cytometry analysis of fluorescence intensity in HeLa cells after incubation with TDN/s-GO using different anchoring methods for 6 h ($n = 3$ biologically independent experiments, with 10 000 cells counted per experiment). (Right) Cytotoxicity assay. (c) Diagram and transmission electron microscope (TEM) snapshots of the phagocytosis process of 37-V/s-GO. Scale bar, 1 μm. (d) Confocal images showing TDN/s-GO (red) and nuclei (blue). Scale bar: 10 μm.

Open Access Article. Published on 09 December 2025. Downloaded on 1/9/2026 8:12:14 PM.
This article is licensed under a Creative Commons Attribution-NonCommercial 3.0 Unported Licence.

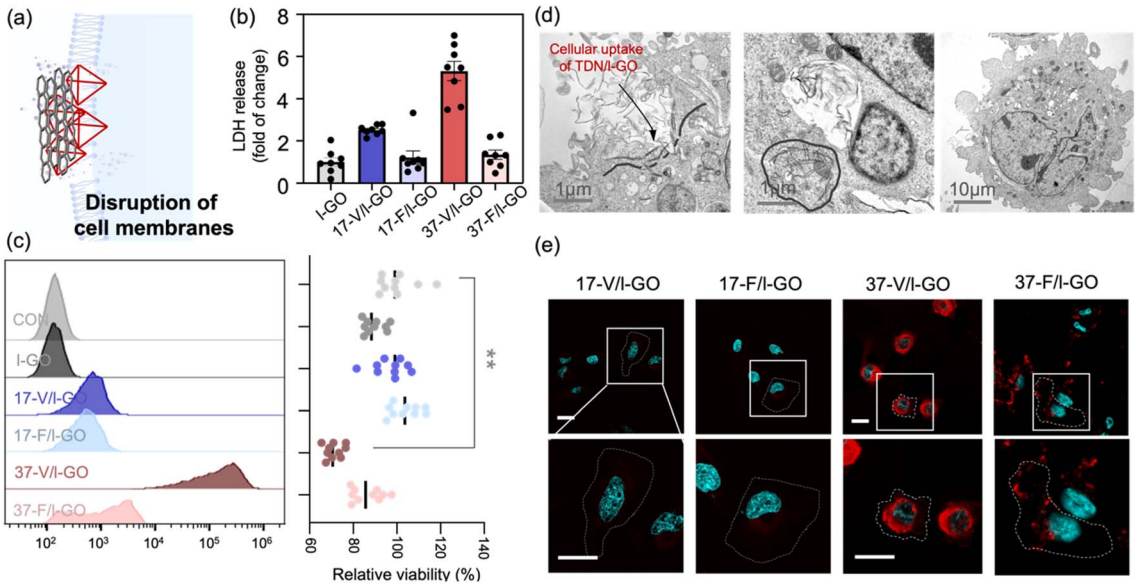

Fig. 6 Cellular internalization pathway of l-GO. (a) Schematic illustration of the large-sized l-GO internalization pathway. (b) The LDH release assay indicates that 37-V/l-GO significantly perturbs the plasma membrane, represented as the mean ± standard deviation (with error bars) from $n = 8$ independent measurements. (c) (Left) Flow cytometry analysis of fluorescence intensity in HeLa cells after incubation with TDN/l-GO using three different anchoring methods for 6 hours ($n = 3$ biologically independent experiments, with 10 000 cells counted per experiment). (Right) Cytotoxicity assay. (d) Diagram and TEM snapshots of the internalization process of 37-V/l-GO. Scale bar, 1 μm. (e) Confocal images showing TDN/l-GO (red) and nuclei (blue). Scale bar, 10 μm.

provided direct structural evidence: 37-V/l-GO adhered tightly to the plasma membrane and generated deep invaginations with localized rupture sites (Fig. 6d and S19).

In contrast, 37-F/l-GO, which minimizes basal-plane contact, showed minimal uptake and negligible membrane perturbation, underscoring its role as a negative control and confirming the specificity of vertex-mediated disruption. Confocal imaging after prolonged incubation (6 h) revealed pronounced vesicle-like protrusions on the cell surface for 37-V/l-GO, consistent with membrane ruffling and injury-repair dynamics (Fig. 6e). These localized permeabilization events may facilitate direct cytosolic access in addition to classical endocytic routes.

Together, these findings indicate that the basal plane of 37-V/l-GO forms a strong membrane-interacting interface, while vertex-displayed TDNs act as focal stress points that destabilize lipid bilayers. This geometry amplifies local mechanical deformation and generates transient nanoscale defects that permit conditional cytosolic entry. Importantly, FRAP recovery of membrane ROIs and preserved cell viability at 12–24 h indicate that this permeabilization remains controlled and repairable at working doses (Fig. S20 and S21).

Overall, these results highlight orientation engineering as a general design principle for tuning cell–material interfaces and enabling DNA-functionalized nanomaterials with programmable intracellular behaviors and therapeutic potential.

Conclusions

In summary, we have established that orientation as a key determinant of how DNA-functionalized nanomaterials interact with cells. By comparing vertex-, line-, and face-displayed TDNs across two sizes and two material platforms, we identified TDN37-Vertex as the most effective configuration for membrane engagement, internalization, and cytosolic access. Its strong performance highlights orientation control as a practical strategy to enhance the delivery of nanomaterials, exosomes, and proteins into cells and tissues.

A coordinated set of measurements—including endocytic mapping, LDH release, TEM visualization, intracellular colocalization, and FRAP recovery—revealed that each orientation produces distinct physical and biological interactions at the membrane. Vertex-displayed TDNs concentrate curvature and stress, accelerating membrane wrapping and uptake. Line-displayed TDNs support multivalent interactions and mixed entry routes. Face-displayed TDNs minimize membrane contact and show low internalization. These consistent trends across PS and GO systems support a geometry-encoded mechanism that governs uptake efficiency, routing, and intracellular fate.

Orientation programming provides a generalizable approach to design nano-bio interfaces with predictable cellular behaviors. Vertex-displayed constructs are suited for cytosolic delivery, intracellular imaging, and therapeutic payload transport due to their strong uptake and escape capacity. Furthermore, the ability of vertex-oriented TDNs on large GO to induce controlled membrane disruption points to potential applications in cancer therapy through oncosis-like processes or in enhancing the delivery of impermeable therapeutics, whereas the low-engagement face orientation may be advantageous for extracellular or membrane-associated uses. Face-displayed structures, with minimal cell entry, are well positioned for membrane monitoring, extracellular sensing, and scenarios requiring sustained lysosomal retention. Line-displayed

 © 2025 The Author(s). Published by the Royal Society of Chemistry

Open Access Article. Published on 09 December 2025. Downloaded on 1/9/2026 8:12:14 PM.
This article is licensed under a Creative Commons Attribution-NonCommercial 3.0 Unported Licence.

formats enable multivalent receptor targeting and immune modulation. These principles extend naturally to diverse nanomaterials through DNA-encoded handle placement, offering a structural basis for building programmable delivery platforms and next-generation biomedical applications.

Author contributions

B. L.: funding acquisition, conceptualization, supervision, writing – review & editing; H. Y.: investigation, formal analysis, writing – original draft; H. L.: investigation, formal analysis, writing – original draft; Z. Z.: formal analysis, writing – review & editing; S. D.: investigation, formal analysis; X. D.: formal analysis.

Conflicts of interest

There are no conflicts to declare.

Data availability

All data supporting this article have been included in the main text or the supplementary information (SI). Supplementary information: experimental, further characterization, fluorescence images, and cellular uptake. See DOI: https://doi.org/10.1039/d5sc08182c.

Acknowledgements

This work was supported by the National Natural Science Foundation of China (No. 22374114 and 32101135), Key Research and Development Program of Shaanxi Province (No. 2023-YBGY-481), and Innovation Capability Support Program of Shaanxi (No. 2023-CX-TD-62). We are grateful to Xiaofei Wang (Biomedical Experimental Center of Xi'an Jiaotong University) and Baochang Lai (Cardiovascular Research Center, School of Basic Medical Sciences, Xi'an Jiaotong University Health Science Center) for their technical support.

Notes and references

1 N. Feliu, D. Docter, M. Heine, P. del Pino, S. Ashraf, J. Kolosnjaj-Tabi, P. Macchiarini, P. Nielsen, D. Alloyeau, F. Gazeau, R. H. Stauber and W. J. Parak, In vivo degeneration and the fate of inorganic nanoparticles, *Chem. Soc. Rev.*, 2016, **45**, 2440–2457.
2 S. Ohta, D. Glancy and W. C. W. Chan, DNA-Controlled Dynamic Colloidal Nanoparticle Systems for Mediating Cellular Interaction, *Science*, 2016, **351**, 841–845.
3 S. Wilhelm, A. J. Tavares, Q. Dai, S. Ohta, J. Audet, H. F. Dvorak and W. C. W. Chan, Analysis of nanoparticle delivery to tumours, *Nat. Rev. Mater.*, 2016, **1**, 16014.
4 S. Behzadi, V. Serpooshan, W. Tao, M. A. Hamaly, M. Y. Alkawareek, E. C. Dreaden, D. Brown, A. M. Alkilany, O. C. Farokhzad and M. Mahmoudi, Cellular uptake of nanoparticles: journey inside the cell, *Chem. Soc. Rev.*, 2017, **46**, 4218–4244.
5 J. J. Rennick, A. P. R. Johnston and R. G. Parton, Key principles and methods for studying the endocytosis of biological and nanoparticle therapeutics, *Nat. Nanotechnol.*, 2021, **16**, 266–276.
6 B. Banushi, S. R. Joseph, B. Lum, J. J. Lee and F. Simpson, Endocytosis in cancer and cancer therapy, *Nat. Rev. Cancer*, 2023, **23**, 450–473.
7 W. Jiang, B. Y. S. Kim, J. T. Rutka and W. C. W. Chan, Nanoparticle-mediated cellular response is size-dependent, *Nat. Nanotechnol.*, 2008, **3**, 145.
8 S. E. A. Gratton, P. A. Ropp, P. D. Pohlhaus, J. C. Luft, V. J. Madden, M. E. Napier and J. M. DeSimone, The effect of particle design on cellular internalization pathways, *Proc. Natl. Acad. Sci. U. S. A.*, 2008, **105**, 11613–11618.
9 J. Wong-Ekkabut, S. Baoukina, W. Triampo, I. M. Tang, D. P. Tieleman and L. Monticelli, Computer simulation study of fullerene translocation through lipid membranes, *Nat. Nanotechnol.*, 2008, **3**, 363–368.
10 J. Zhou and J. Rossi, Aptamers as targeted therapeutics: current potential and challenges, *Nat. Rev. Drug Discovery*, 2016, **16**, 181.
11 Y. C. Zeng, O. J. Young, C. M. Wintersinger, F. M. Anastassacos, J. I. MacDonald, G. Isinelli, M. O. Dellacherie, M. Sobral, H. Bai, A. R. Graveline, A. Vernet, M. Sanchez, K. Mulligan, Y. Choi, T. C. Ferrante, D. B. Keskin, G. G. Fell, D. Neuberg, C. J. Wu, D. J. Mooney, I. C. Kwon, J. H. Ryu and W. M. Shih, Fine tuning of CpG spatial distribution with DNA origami for improved cancer vaccination, *Nat. Nanotechnol.*, 2024, **19**, 1055–1065.
12 M. J. Mitchell, M. M. Billingsley, R. M. Haley, M. E. Wechsler, N. A. Peppas and R. Langer, Engineering precision nanoparticles for drug delivery, *Nat. Rev. Drug Discovery*, 2021, **20**, 101–124.
13 K. Huang, Q. Yang, M. Bao, S. Wang, L. Zhao, Q. Shi and Y. Yang, Modulated Cell Internalization Behavior of Icosahedral DNA Framework with Programmable Surface Modification, *J. Am. Chem. Soc.*, 2024, **146**, 21442–21452.
14 Y. Tokura, S. Harvey, C. Chen, Y. Wu, D. Y. W. Ng and T. Weil, Fabrication of Defined Polydopamine Nanostructures by DNA Origami-Templated Polymerization, *Angew. Chem., Int. Ed.*, 2018, **57**, 1587–1591.
15 R. P. Goodman, R. M. Berry and A. J. Turberfield, The single-step synthesis of a DNA tetrahedron, *Chem. Commun.*, 2004, 1372–1373, DOI: 10.1039/B402293A.
16 J. Zhang, Y. Guo, F. Ding, G. Pan, X. Zhu and C. Zhang, A Camptothecin-Grafted DNA Tetrahedron as a Precise Nanomedicine to Inhibit Tumor Growth, *Angew. Chem., Int. Ed.*, 2019, **58**, 13794–13798.
17 F. Yin, M. Li, X. Mao, F. Li, X. Xiang, Q. Li, L. Wang, X. Zuo, C. Fan and Y. Zhu, DNA Framework-Based Topological Cell Sorters, *Angew. Chem., Int. Ed.*, 2020, **59**, 10406–10410.
18 T. Zhang, T. Tian, R. Zhou, S. Li, W. Ma, Y. Zhang, N. Liu, S. Shi, Q. Li, X. Xie, Y. Ge, M. Liu, Q. Zhang, S. Lin, X. Cai and Y. Lin, Design, fabrication and applications of tetrahedral DNA nanostructure-based multifunctional

Open Access Article. Published on 09 December 2025. Downloaded on 1/9/2026 8:12:14 PM.
This article is licensed under a Creative Commons Attribution-NonCommercial 3.0 Unported Licence.

complexes in drug delivery and biomedical treatment, *Nat. Protoc.*, 2020, **15**, 2728–2757.

19 W. Wang, M. Lin, W. Wang, Z. Shen and Z.-S. Wu, DNA tetrahedral nanostructures for the biomedical application and spatial orientation of biomolecules, *Bioact. Mater.*, 2024, **33**, 279–310.

20 H. Zhao, D. Yi, L. Li, Y. Zhao and M. Li, Modular Weaving DNAzyme in Skeleton of DNA Nanocages for Photoactivatable Catalytic Activity Regulation, *Angew. Chem., Int. Ed.*, 2024, **63**, e202404064.

21 Y. Ren, Z. Zhou, K. Maxeiner, A. Kaltbeitzel, I. Harley, J. Xing, Y. Wu, M. Wagner, K. Landfester, I. Lieberwirth, T. Weil and D. Y. W. Ng, Supramolecular Assembly in Live Cells Mapped by Real-Time Phasor-Fluorescence Lifetime Imaging, *J. Am. Chem. Soc.*, 2024, **146**, 11991–11999.

22 J. Li, X. Mao, T. Zhao, W. Fang, Y. Jin, M. Liu, C. Fan and Y. Tian, Tetrahedral DNA Framework-Based Spherical Nucleic Acids for Efficient siRNA Delivery, *Angew. Chem., Int. Ed.*, 2025, **64**, e202416988.

23 A. Fischer, P. Zhang, Y. Ouyang, Y. S. Sohn, O. Karmi, R. Nechushtai, E. Pikarsky and I. Willner, DNA-Tetrahedra Corona-Modified Hydrogel Microcapsules: "Smart" ATP- or microRNA-Responsive Drug Carriers, *Small*, 2024, **18**, 2204108.

24 P. Zhang, A. Fischer, Y. Ouyang, J. Wang, Y. S. Sohn, R. Nechushtai, E. Pikarsky, C. Fan and I. Willner, Aptamer-modified DNA tetrahedra-gated metal–organic framework nanoparticle carriers for enhanced chemotherapy or photodynamic therapy, *Chem. Sci.*, 2021, **12**, 14473–14483.

25 P. Zhang, Y. Ouyang, Y. S. Sohn, R. Nechushtai, E. Pikarsky, C. Fan and I. Willner, pH- and miRNA-Responsive DNA-Tetrahedra/Metal–Organic Framework Conjugates: Functional Sense-and-Treat Carriers, *ACS Nano*, 2021, **15**, 6645–6657.

26 J. Li, K. Xun, L. Zheng, X. Peng, L. Qiu and W. Tan, DNA-Based Dynamic Mimicry of Membrane Proteins for Programming Adaptive Cellular Interactions, *J. Am. Chem. Soc.*, 2021, **143**, 4585–4592.

27 Y.-H. Ma, Y. Zhu, H. Wu, Y. He, Q. Zhang, Q. Huang, Z. Wang, H. Xing, L. Qiu and W. Tan, Domain-Targeted Membrane Partitioning of Specific Proteins with DNA Nanodevices, *J. Am. Chem. Soc.*, 2024, **146**, 7640–7648.

28 A. Lacroix, E. Vengut-Climent, D. de Rochambeau and H. F. Sleiman, Uptake and Fate of Fluorescently Labeled DNA Nanostructures in Cellular Environments: A Cautionary Tale, *ACS Cent. Sci.*, 2019, **5**, 882–891.

29 C. J. Whitfield, M. Zhang, P. Winterwerber, Y. Wu, D. Y. W. Ng and T. Weil, Functional DNA–Polymer Conjugates, *Chem. Rev.*, 2021, **121**, 11030–11084.

30 L. Liang, J. Li, Q. Li, Q. Huang, J. Shi, H. Yan and C. Fan, Single-Particle Tracking and Modulation of Cell Entry Pathways of a Tetrahedral DNA Nanostructure in Live Cells, *Angew. Chem., Int. Ed.*, 2014, **53**, 7745–7750.

31 H. Ding, J. Li, N. Chen, X. Hu, X. Yang, L. Guo, Q. Li, X. Zuo, L. Wang, Y. Ma and C. Fan, DNA Nanostructure-Programmed Like-Charge Attraction at the Cell-Membrane Interface, *ACS Cent. Sci.*, 2018, **4**, 1344–1351.

32 X. Peng, S. Fang, B. Ji, M. Li, J. Song, L. Qiu and W. Tan, DNA Nanostructure-Programmed Cell Entry *via* Corner Angle-Mediated Molecular Interaction with Membrane Receptors, *Nano Lett.*, 2021, **21**, 6946–6951.

33 M. Lin, J. Wang, G. Zhou, J. Wang, N. Wu, J. Lu, J. Gao, X. Chen, J. Shi, X. Zuo and C. Fan, Programmable Engineering of a Biosensing Interface with Tetrahedral DNA Nanostructures for Ultrasensitive DNA Detection, *Angew. Chem., Int. Ed.*, 2015, **54**, 2151–2155.

34 Y. Tian, Y. Zhang, T. Wang, H. L. Xin, H. Li and O. Gang, Lattice engineering through nanoparticle-DNA frameworks, *Nat. Mater.*, 2016, **15**, 654–661.

35 K. E. Bujold, A. Lacroix and H. F. Sleiman, DNA Nanostructures at the Interface with Biology, *Chem*, 2018, **4**, 495–521.

36 J. J. Rennick, A. P. R. Johnston and R. G. Parton, Key principles and methods for studying the endocytosis of biological and nanoparticle therapeutics, *Nat. Nanotechnol.*, 2021, **16**, 266–276.

37 M. Kollaschinski, J. Sobotta, A. Schalk, T. Frischmuth, B. Graf and S. Serdjukow, Efficient DNA Click Reaction Replaces Enzymatic Ligation, *Bioconjugate Chem.*, 2020, **31**, 507–512.

38 J. E. Gestwicki, C. W. Cairo, L. E. Strong, K. A. Oetjen and L. L. Kiessling, Influencing Receptor–Ligand Binding Mechanisms with Multivalent Ligand Architecture, *J. Am. Chem. Soc.*, 2002, **124**, 14922–14933.

39 Z. Xia, P. Wang, X. Liu, T. Liu, Y. Yan, J. Yan, J. Zhong, G. Sun and D. He, Tumor-Penetrating Peptide-Modified DNA Tetrahedron for Targeting Drug Delivery, *Biochemistry*, 2016, **55**, 1326–1331.

40 Y. Du, P. Peng and T. Li, DNA Logic Operations in Living Cells Utilizing Lysosome-Recognizing Framework Nucleic Acid Nanodevices for Subcellular Imaging, *ACS Nano*, 2019, **13**, 5778–5784.

41 M. Li, H. Ding, M. Lin, F. Yin, L. Song, X. Mao, F. Li, Z. Ge, L. Wang, X. Zuo, Y. Ma and C. Fan, DNA Framework-Programmed Cell Capture *via* Topology-Engineered Receptor–Ligand Interactions, *J. Am. Chem. Soc.*, 2019, **141**, 18910–18915.

42 C. Wiraja, Y. Zhu, D. C. S. Lio, D. C. Yeo, M. Xie, W. Fang, Q. Li, M. Zheng, M. Van Steensel, L. Wang, C. Fan and C. Xu, Framework nucleic acids as programmable carrier for transdermal drug delivery, *Nat. Commun.*, 2019, **10**, 1147.

43 J. Gačanin, C. V. Synatschke and T. Weil, Biomedical Applications of DNA-Based Hydrogels, *Adv. Funct. Mater.*, 2020, **30**, 1906253.

44 A. Lacroix and H. F. Sleiman, DNA Nanostructures: Current Challenges and Opportunities for Cellular Delivery, *ACS Nano*, 2021, **15**, 3631–3645.

45 A. Lesniak, A. Salvati, M. J. Santos-Martinez, M. W. Radomski, K. A. Dawson and C. Åberg, Nanoparticle Adhesion to the Cell Membrane and Its Effect on Nanoparticle Uptake Efficiency, *J. Am. Chem. Soc.*, 2013, **135**, 1438–1444.

 © 2025 The Author(s). Published by the Royal Society of Chemistry

Open Access Article. Published on 09 December 2025. Downloaded on 1/9/2026 8:12:14 PM.
This article is licensed under a Creative Commons Attribution-NonCommercial 3.0 Unported Licence.

46 P. Choo, T. Liu and T. W. Odom, Nanoparticle Shape Determines Dynamics of Targeting Nanoconstructs on Cell Membranes, *J. Am. Chem. Soc.*, 2021, **143**, 4550–4555.

47 C. Liang, Q. Huang, H. Zheng, M. Duan, X. Cheng, J. Chen, Q. Li, Z. Zhang, C. Fan, H. Tian and J. Shen, Probing Cell Membrane Tension Using DNA Framework-Encoded Vibration-Induced Emission Molecular Assemblies, *J. Am. Chem. Soc.*, 2024, **146**, 34341–34351.

48 A. K. Geim and K. S. Novoselov, The Rise of Graphene, *Nat. Mater.*, 2007, **6**, 183–191.

49 G. Peng, H. M. Sinkko, H. Alenius, N. Lozano, K. Kostarelos, L. Bräutigam and B. Fadeel, Graphene oxide elicits microbiome-dependent type 2 immune responses *via* the aryl hydrocarbon receptor, *Nat. Nanotechnol.*, 2023, **18**, 42–48.

50 E. Zhu, J. Yu, Y.-R. Li, F. Ma, Y.-C. Wang, Y. Liu, M. Li, Y. J. Kim, Y. Zhu, Z. Hahn, Y. Zhou, J. Brown, Y. Zhang, M. Pelegrini, T. Hsiai, L. Yang and Y. Huang, Biomimetic cell stimulation with a graphene oxide antigen-presenting platform for developing T cell-based therapies, *Nat. Nanotechnol.*, 2024, **19**, 1914–1922.

51 H. Hillaireau and P. Couvreur, Nanocarriers' entry into the cell: relevance to drug delivery, *Cell. Mol. Life Sci.*, 2009, **66**, 2873–2896.

52 X. Liu and K. L. Chen, Interactions of Graphene Oxide with Model Cell Membranes: Probing Nanoparticle Attachment and Lipid Bilayer Disruption, *Langmuir*, 2015, **31**, 12076–12086.

53 Z. Guo, P. Zhang, C. Xie, E. Voyiatzis, K. Faserl, A. J. Chetwynd, F. A. Monikh, G. Melagraki, Z. Zhang, W. J. G. M. Peijnenburg, A. Afantitis, C. Chen and I. Lynch, Defining the Surface Oxygen Threshold That Switches the Interaction Mode of Graphene Oxide with Bacteria, *ACS Nano*, 2023, **17**, 6350–6361.